UDK 542.65:661.865.5
Original scientific article/Izvirni znanstveni članek

ISSN 1580-2949
MTAEC9, 56(5)453(2022)

INFLUENCE OF Ce ADDITION ON THE MICROSTRUCTURE AND HOT-PROCESSING MAPS OF Mg-1Ca-0.5Mn ALLOYS

VPLIV DODATKA Ce NA MIKROSTRUKTURO IN PROCESNE MAPE VROČEGA ZGOŠČEVANJA ZLITIN Mg-1Ca-0,5Mn

Zhihui Cai[1,2], Yongyong Jia[1], Qinhong Fan[1,2], Yaojie Hou[1], Lifeng Ma[1*]

[1]School of Mechanical Engineering, Taiyuan University of Science and Technology, Taiyuan, China
[2]Heavy Machinery Engineering Research Center of the Ministry of Education, Taiyuan University of Science and Technology, Taiyuan, China

Prejem rokopisa – received: 2022-04-28; sprejem za objavo – accepted for publication: 2022-07-07

doi:10.17222/mit.2022.489

To investigate the processability of Mg-1Ca-0.5Mn alloys with and without the addition of Ce, hot-compression tests were performed on a Gleeble-3800 thermo-mechanical simulator at 300–450 °C and 0.001–5 s^{-1}. The flow stress, processing map, and microstructure characterization of the alloys were investigated. The results show that the flow stress of the Mg-1Ca-0.5Mn-0.5Ce alloy was significantly improved for all the thermomechanical deformation parameters, and the dynamic recrystallization phenomenon was delayed. This phenomenon was attributed to the finer grains and the dense distribution of the fine and coarse particles pinned at the grain boundaries. The processing map shows that the Mg-1Ca-0.5Mn-0.5Ce alloy has better processing performance at a low strain rate.

Keywords: Mg-Ca-Mn alloy, Ce addition, hot compression, processing map

Avtorji v članku opisujejo raziskavo o procesiranju zlitine Mg-1Ca-0.5Mn brez in z dodatkom cerija (Ce). Izvajali so primerjalne teste vročega tlačnega stiskanja na termomehanskem simulatorju Gleeble-3800 pri temperaturah med 300 °C in 450 °C ter hitrostih deformacije med 0.001 s^{-1} in 5 s^{-1}. Določili so krivulje tečenja, izdelali procesni mapi in analizirali mikrostrukturo obeh preiskovanih zlitin. Rezultati raziskave so pokazali, da se je napetost tečenja zlitine z dodatkom cerija Mg-1Ca-0,5Mn-0,5Ce močno izboljšala (povišala) in prav tako vsi ostali termomehanski deformacijski parametri z zakasnitvijo pojava dinamične rekristalizacije. Avtorji članka ta pojav pripisujejo nastanku finejših (bolj drobnih) kristalnih zrn in gostejši porazdelitvi finih in grobih delcev pripetih na meje kristalnih zrn. Izdelana procesna mapa je pokazala, da ima zlitina Mg-1Ca-0.5Mn-0,5Ce boljše procesne lastnosti pri nižji hitrosti deformacije.

Ključne besede: zlitina na osnovi Mg, Ca in Mn, dodatek Ce, vroče zgoščevanje, procesna mapa

1 INTRODUCTION

As the lightest engineering material, magnesium (Mg) alloys have a series of excellent properties, such as high specific strength, anti-fatigue, high damping, and shock absorption, so it has a broad application prospect in the fields of aerospace and automotive.[1,2] However, Mg alloys have poor mechanical properties due to their dense hexagonal structure, which severely limits their widespread application.[3] Therefore, these alloys have attracted plenty of researchers to explore ways to improve the ductility of Mg alloys.

It is well known that alloying can improve the strength and plasticity of materials. In recent years, many researchers have investigated the effect of alloying of Ca and Mn elements on the properties of Mg alloys.[4–6] For example, Jiang et al.[7] found that the grain size and density of the precipitates in the extruded Mg-2Zn-xCa (*w*/%) alloy increased with increasing Ca content, resulting in increased strength of the alloy. Similarly, by modifying the Mn content, an ultra-high, as-extruded Mg-5.5Al-3Ca-0.3Mn alloy with a yield strength (YS) of 402 MPa was successfully developed.[8] However, while the strength of the alloys with Ca and Mn elements was significantly increased (YS > 351 MPa), the ductility of these alloys was much lower (< 10 %). In addition, low-cost Ce rare-earth elements were reported to significantly improve the properties of the alloy. Y. Du et al. reported that the elongation of Mg-3Zn was enhanced from 24 % to 35 % after 0.05 *w*/% Ce addition.[9] Hence, it is necessary to explore the effect of combined additions of Ca, Mn, and Ce on the mechanical properties and microstructures in Mg-1Ca-0.5Mn alloys.

At present, most studies have focused on the influence of extruded alloys, but the rolled Mg-Ca-Mn alloy has not been investigated. Therefore, it is necessary to study the thermomechanical deformation behavior of the alloy before rolling to obtain the best processing range to guide the subsequent rolling experiments. To optimize the thermomechanical deformation process parameters, the process parameters such as temperatures, strains, and strain rates with optimized microstructure and mechanical properties are directly linked by the processing map.[10,11] Scott C. Sutton et al.[12] studied the constitutive behavior and processing maps of a new wrought Mg alloy ZE20 (Mg-2Zn-0.2Ce) and revealed that a safe region for processing occurs between 375 °C and 450 °C,

*Corresponding author's e-mail:
tsaizhihui@163.com (Z. H. Cai)

from 0.003 s^{-1} to 0.1 s^{-1}. In this work the influence of Ce addition on the microstructure, hot-processing maps of Mg-1Ca-0.5Mn alloys was investigated.

2 EXPERIMENTAL PART

The materials used in this study were cast Mg-1Ca-0.5Mn and Mg-1Ca-0.5Mn-0.5Ce alloys. The compositions are shown in **Table 1**. And the Mg-1Ca-0.5Mn alloy and Mg-1Ca-0.5Mn-0.5Ce alloys were encoded as XM10 and XME100 samples, respectively. The as-received alloy was homogenized at 420 °C for 12 h to promote microstructural uniformity. The sample size used for the thermal compression experiment is a cylinder with a length of 15 mm and a diameter of 10 mm. The uniaxial isothermal compression test was carried out on the Gleeble-3800 testing machine. The compressive deformation processes are shown in **Figure 1**. Hot-compression conditions are as follows: deformation temperature in the range 300–450 °C, strain rate 0.001–5 s^{-1}, and the relative pressure reduction of the sample was 60 %. The sample was heated to the deformation temperature at a heating rate of 5 K/s, kept for 5 min, and then subjected to compression, followed by quenching to retain the hot-deformation structure.

Table 1: Chemical compositions of XM10 and XME100 alloy (*w*/%)

	Alloy	Mn	Ca	Ce	Mg
XM10	Mg-1Ca-0.5Mn	0.49	1.12	–	Bal.
XME100	Mg-1Ca-0.5Mn-0.5Ce	0.50	1.00	0.53	Bal.

The microstructure under different processing parameters was characterized by optical microscopy (OM, PMG3, OLYMPUS, Tokyo, Japan) and scanning electron microscopy (SEM, Zeiss, Sigma 500). The phase component was confirmed by energy-dispersive spectrometry (EDS, Zeiss, Sigma 500) with 15 kV and the working distance of 12.5 mm. The metallographic specimens were ground on 400, 800, and 1000 grit silicon carbide paper, followed by grinding on waterproof abrasive paper. Then the samples were etched for OM and SEM with an acetic glycol solution (60 mL ethylene glycol, 10 mL acetic acid) containing saturated picric acid.

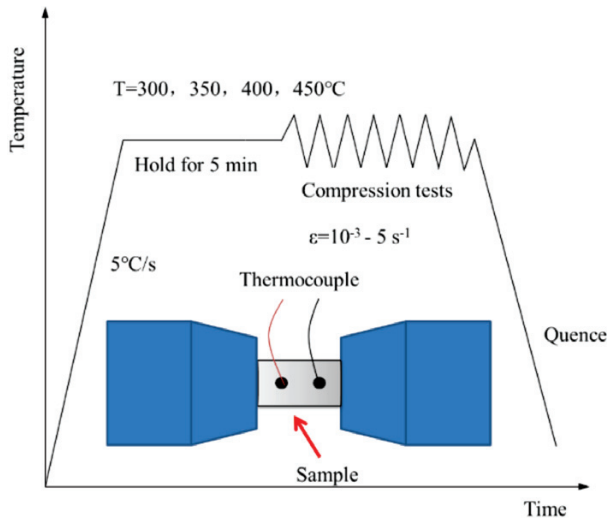

Figure 1: Schematic diagram and specimen geometry of the hot-compression test

3 RESULTS AND DISCUSSION

3.1 Flow characteristics and deformation mechanisms

The experimental flow curves under different deformation parameters are shown in **Figure 2**. The solid line represents the XM10 alloy, and the dashed line represents the XME100 alloy. The deformation curves of the two alloys exhibit typical thermomechanical deformation behavior, with the values of the flow stress proportional to the strain rate and inversely proportional to the temperature. Moreover, the flow stress of the XME100 alloy was significantly improved with the addition of Ce. For example, the flow stress of the XME100 alloy at 1 s^{-1} was comparable to that of XM10 alloy at 5 s^{-1}. And obvious softening was observed in the XME100 alloy at 450 °C and 5 s^{-1}. These phenomena can be attributed to the addition of Ce, which could refine the grains as well as promote the precipitation of the second phase and the occurrence of dynamic recrystallization (DRX). In addition, it can be seen from **Figure 2** that the curves can be divided into three types according to the changing trend of the curves:

The trend of the flow stress curve for both alloys approximates to a constant straight line, which can be regarded as ideal plastic flow at 400–450 °C and 0.01 s^{-1}. The temperature of 400–450 °C corresponds to 62–70 % of the melting point of Mg (648 °C), which means that the thermomechanical deformation of the alloy is less hampered in this temperature range. When the strain rate is low, the deformation of the alloy is unrestricted, resulting in a flat curve. And this phenomenon also appears at 350–450 °C and 0.001 s^{-1}.

The flow stress at 350–450 °C and 1 s^{-1} first rises to a peak and then decreases slightly. This behavior is classically attributed to dynamic recovery (DRV), and the stress increase with the increase of the strain. Moreover, the slight decrease of the flow stress at high strain is attributed to the occurrence of DRX. And the interaction between DRX and DRV leads to the phenomenon in the figure.

The flow stress rises to peak value, followed by significant flow softening at 450 °C and 5 s^{-1}. The curve shows an obvious rising trend of hardening until they reach peak stress, after which the trend of significant softening down related to DRX is observed.

The true stress-strain curves of the XM10 and XME100 alloys at different temperatures with 0.001 s^{-1} strain rates are shown in **Figure 3**. It was found that the peak value of the curves lagged after Ce was added into the XM10 alloy at 0.001 s^{-1}. By a simple inspection of

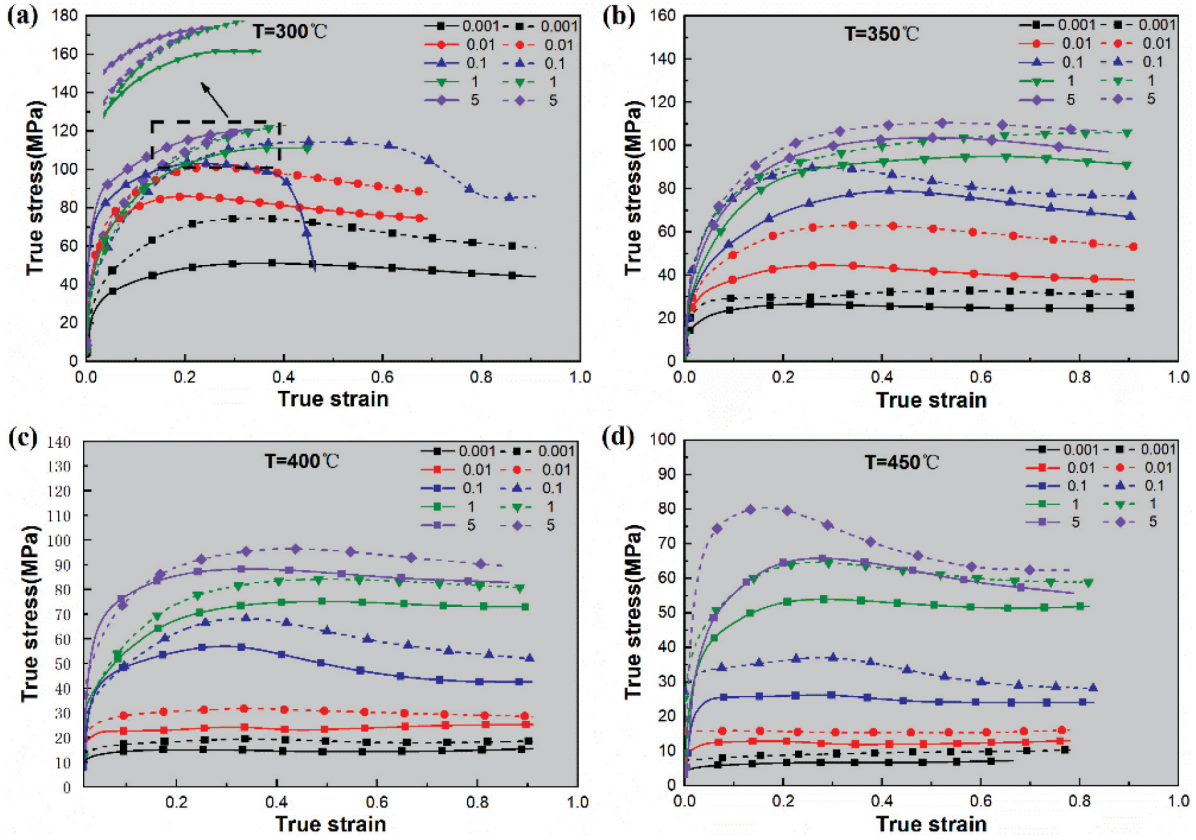

Figure 2: True stress-strain curves for alloys: a) 300 °C, b) 350 °C, c) 400 °C, d) 450 °C

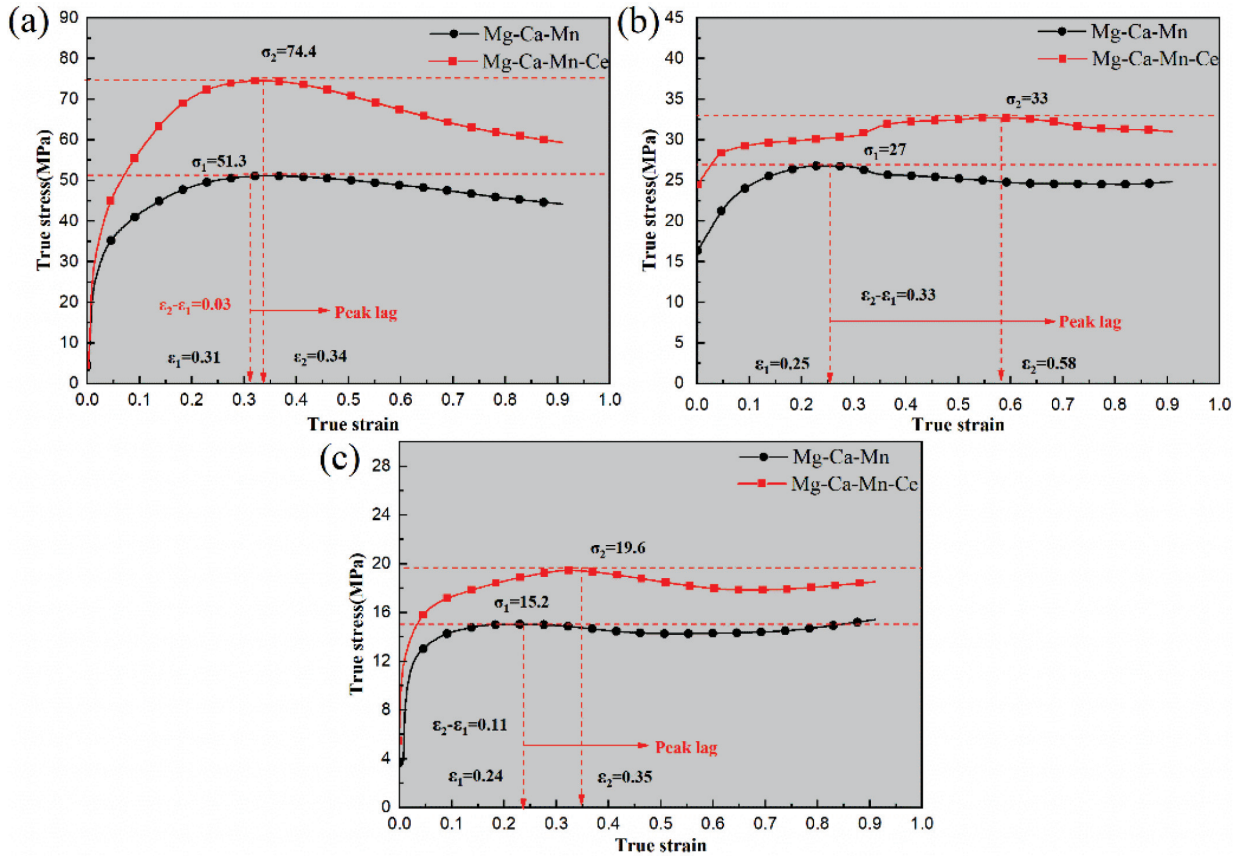

Figure 3: True stress-strain curves for alloys: a) 300 °C, 0.001 s^{-1}, b) 350 °C, 0.001 s^{-1}, c) 400 °C, 0.001 s^{-1}

Figure 3, the XM10 alloy reaches the peak stress at strains of 0.31, 0.25, and 0.24, respectively. The XME100 alloy reached peak stresses of 74.4 MPa, 33 MPa, and 19.6 MPa at strains of 0.34, 0.58, and 0.35, respectively. This may be since the addition of Ce is not conducive to the initiation of the slip system, reducing the slip and block of dislocations, thereby preventing the occurrence of DRX. This phenomenon will be further explained in Section 3.3.

3.2 Processing maps and characterization

The processing map was a graph that characterizes the inherent processing properties of the materials through different strain rates, strain, and temperatures. It was based on the DMM first developed by Wellstead and improved by Prasad et al.[13–15] Modeling the deformation process of the sample as linear power dissipation by the principles of the DMM, and an instability criterion subsequently superimposed. Thus, a stable processing zone for the workpiece processing is obtained.

Figure 4 shows the 3D power-dissipation map under different strains to explore the influence of different deformation parameters on the power-dissipation value. As shown in **Figures 4a** to **4c** the power-dissipation efficiency increases from 0.34 to 0.38 with the increase of strain from 0.15 to 0.25. Then, the efficiency of the power dissipation decreases sharply from 0.38 to 0.14 with an increase in strain from 0.25 to 0.35. A higher η value has better processing performance, which indicates that the workability under 0.35 strain of the alloy becomes narrower. The sudden drop of the power dissipation value around 0.35 true strains at 350 °C and 0.001 s^{-1} might be caused by defects within the material. It can be seen from **Figures 4d** to **4f** that the peak power-dissipation efficiency of the XEM100 alloy and the region of η values greater than 0.35 increase with the increase of strain. The higher power-dissipation coefficient in the XME100 alloy is distributed in the low-strain-rate region and high temperature.

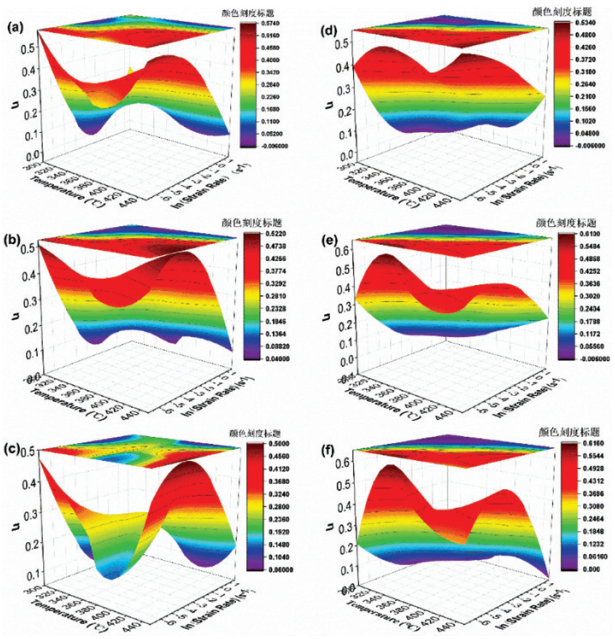

Figure 4: Power-dissipation maps of alloys: a) XM10, strain 0.15, b) XME100, strain 0.15 c) XM10, strain 0.25, d) XME100, strain 0.25, e) XM10, strain 0.35), f) XME100, strain 0.35

The η value represents the ratio of the energy consumed due to microstructural evolution to the total energy consumed linearly during the heat-deformation process. Phenomena such as DRV or DRX were often found in areas with high η values. It was generally accepted that the alloy has better processability at the temperature and strain rate of DRX. According to the stacking-fault energy of the material, the DRX usually occurs between 30 % and 55 %.[16] The power-dissipation value of the alloy increases with the increase of the strain at a low strain rate. The main reason is the density of the dislocations in the grains increases with the increase of strain, resulting in dislocation recombination, climbing, and other behavior. Meanwhile, the accumulation of dislocations is conducive to accelerating the occurrence of DRX. Especially at low strain rate, there is enough time for DRX and grain growth, thus more recrystallized grains are produced, more deformation energy is consumed, and a higher power-dissipation value is shown.[17] So, the alloy with Ce possesses better processing performance, especially at low temperature and low strain compared with XM10 alloy.

Figure 5 shows the processing maps of the XM10 and XEM100 alloys at different strains. The stable and unstable regions are marked with rectangular frames and symbols, respectively. It can be seen from **Figures 5a** to **5c** that in XM10 alloy, under the strain of 0.15, region I exist between 390 °C and 450 °C below 0.2 s^{-1}. Region II exists between 370 °C and 415 °C below 0.004 s^{-1}. When the strain reaches 0.25, a new stable region appears at low temperature and low strain rate. However, this area is so tiny that it cannot be accurately used for actual processing. When the strain reaches 0.3, in the medium-temperature and low-strain region (temperature 380–415 °C, strain rate less than 0.0015 s^{-1}), there is an unstable region II, which is extremely detrimental to the processing of the sample. In the XME100 alloy, it can be seen from **Figures 5d** to **5f** that when the strain is 0.15, the image shows two stable regions, which are located at the low- and medium-temperature strain rate (temperature 300–390 °C, strain rate less than 0.0025 s^{-1}) and high-temperature medium strain rate (temperature is 420–450 °C, and the strain rate is less than 0.082 s^{-1}), which are respectively represented as processable areas I and II. As the strain increases to 0.25, a new stable region appears in the high-temperature and low-strain area, which indicates that the alloy has good processing ability under low strain, and this area is collectively referred to as the stable region I, located at a temperature of 300–450 °C, the strain rate is less than 0.004 s^{-1}. Stable

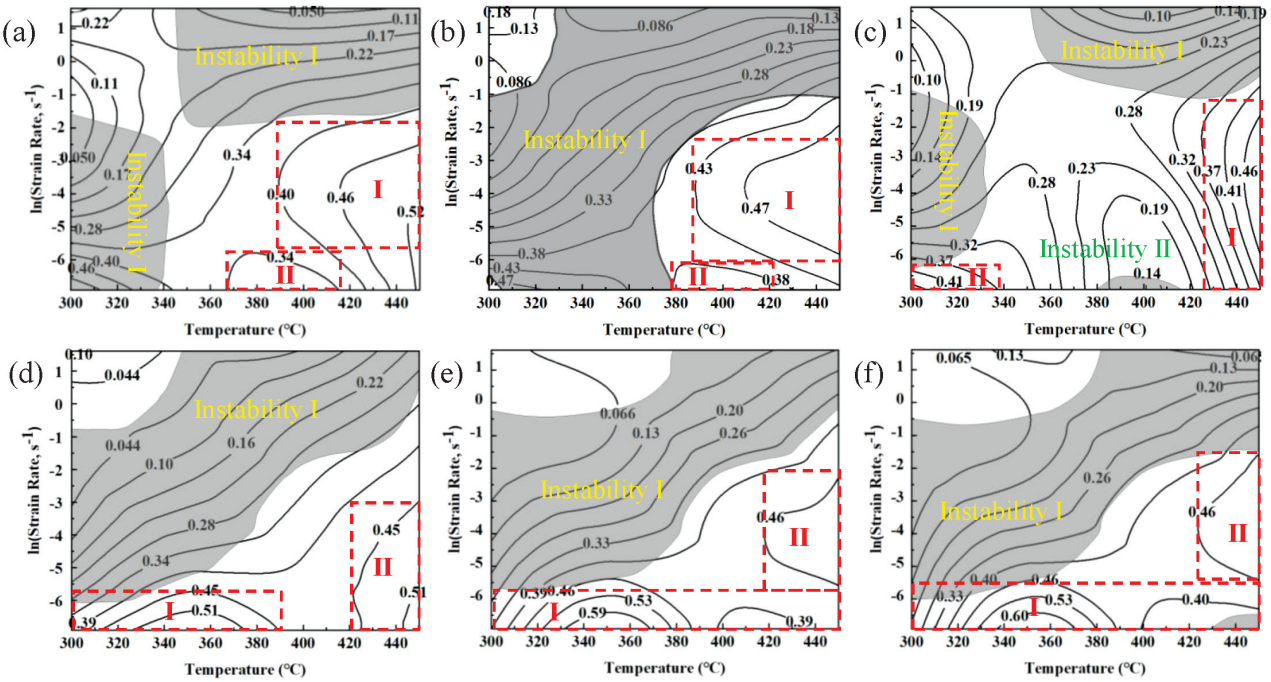

Figure 5: Processing maps for alloys: a) XM10, strain 0.15, b) XM10, strain 0.25, c) XM10, strain 0.35, d) XME100, strain 0.15, e) XME100, strain 0.25, f) XME100, strain 0.35

region II is located at a temperature of 418–450 °C and a strain rate of 0.003–0.1 s^{-1}. When the strain is 0.35, the processable area is expanded to a temperature of 400–450 °C, and the strain rate is 0.0035–0.5 s^{-1}.

Therefore, the XME100 alloy with added Ce has better machinability. It not only has high power-dissipation values and a stable workable region at low strain rates, but also has a good workable interval at high temperatures and high strain rates. Since the low strain rates are not suitable for the actual industrial production, the best optimal processing region selected is the stable region II, the temperature is 400–450 °C, and the strain rate is 0.0035–0.5 s^{-1}.

3.3 Effect of Ce element on microstructure

The peak value of the stress-strain curves indicates the dynamic equilibrium of DRX and strain hardening of the alloy. The hysteresis of the stress peak indicates the enhancement of strain hardening or the weakening of the DRX effect.[18]

The strain-hardening capacity (HC) of a metallic material is one of the important considerations in the analysis of the strain-hardening effect.[19,20] Therefore, Equation (1) for HC was as follows:

$$HC = \frac{\sigma_{ucs}^{true} - \sigma_{0.2}^{true}}{\sigma_{0.2}^{true}} = \frac{\sigma_{ucs}^{true}}{\sigma_{0.2}^{true}} - 1 \qquad (1)$$

Where $\sigma_{0.2}^{true}$ is the true YS and σ_{ucs}^{true} represents the true ultimate compressive strength (UCS). The calculation results are shown in **Table 2**. The HC value of the XME100 alloy is lower than that of the XM10 alloy, indicating the weaker strain-hardening effect. To sum up, the peak stress lagged of the alloy may be the result of the weakening of both strain hardening and DRX, but it has a more remarkable influence on the strain hardening.

Table 2: Strain-hardening capacity of XM10 and XME100 alloys

Alloy	HC
XM10	0.82222
XME100	0.53752

Figure 6 shows the microstructures of the as-cast XM10 alloy and XME100 alloys. The OM image of the XM10 alloy showed a coarse microstructure, with a substantial presence of precipitate phase, and the XME100 alloy has a finer grain with the addition of Ce. It is generally accepted that the strength and plasticity of an alloy increase with the decrease in grain size. The strength of the alloy is enhanced due to the smaller grain size, which leads to an increase of grain boundaries in the alloy. The occurrence of dislocation slip needs to pass through the grain boundary, thus the alloy with fine grains has a higher strength. The mechanism of improving the plasticity is as follows. The number of grains in a certain volume increases with the decrease of the grain size. Under a certain plastic deformation, the average deformation in each grain is less, which makes the probability of grain cracking smaller, leading to the enhancement of the plasticity. In addition, fine grains may explain the change in the strain hardening of the alloy. U.F. Kocks et al.[21] reported that the grain size significantly affects the strain-hardening behavior and the grain refinement weakens the effect of the strain hardening. Many schol-

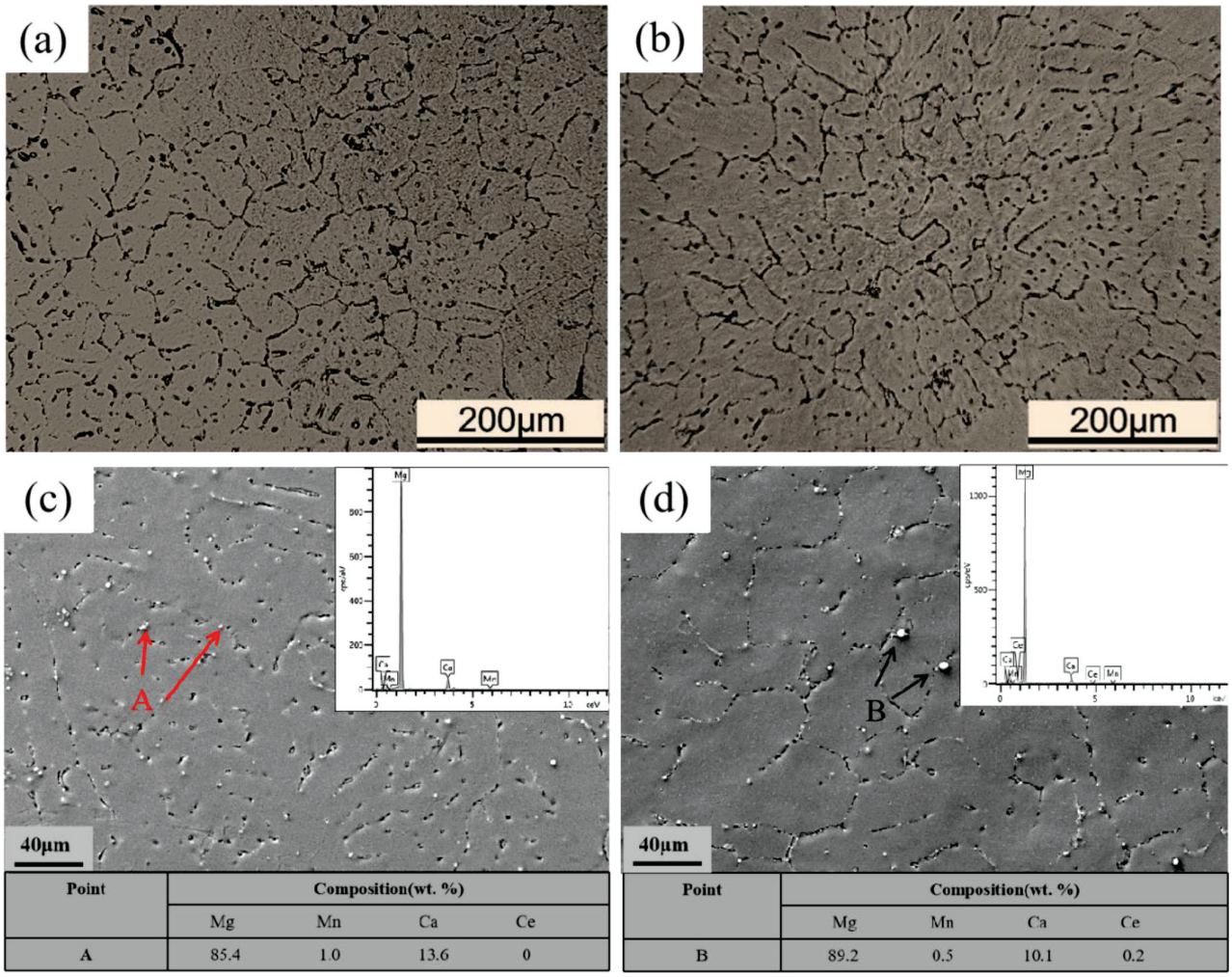

Point	Composition(wt. %)			
	Mg	Mn	Ca	Ce
A	85.4	1.0	13.6	0

Point	Composition(wt. %)			
	Mg	Mn	Ca	Ce
B	89.2	0.5	10.1	0.2

Figure 6: Microstructures of as-cast alloys: a) XM10, OM, b) XME100, OM, c) XM10, SEM, d) XME100, SEM

ars have also reported that grain refinement can weaken the ability of work hardening.[22,23] This phenomenon may be attributed to the reduction of the maximum dislocation density in the grains due to grain refinement, which leads to the reduction of the work-hardening capacity.

As we can see in **Figures 6c** and **6d**, many second-phase particles appear on the grain boundaries of the two alloys. The difference is that the fine precipitates are mainly distributed in the XM10 alloy, while some coarse second-phase particles appear in the XME100 alloy. Ac-

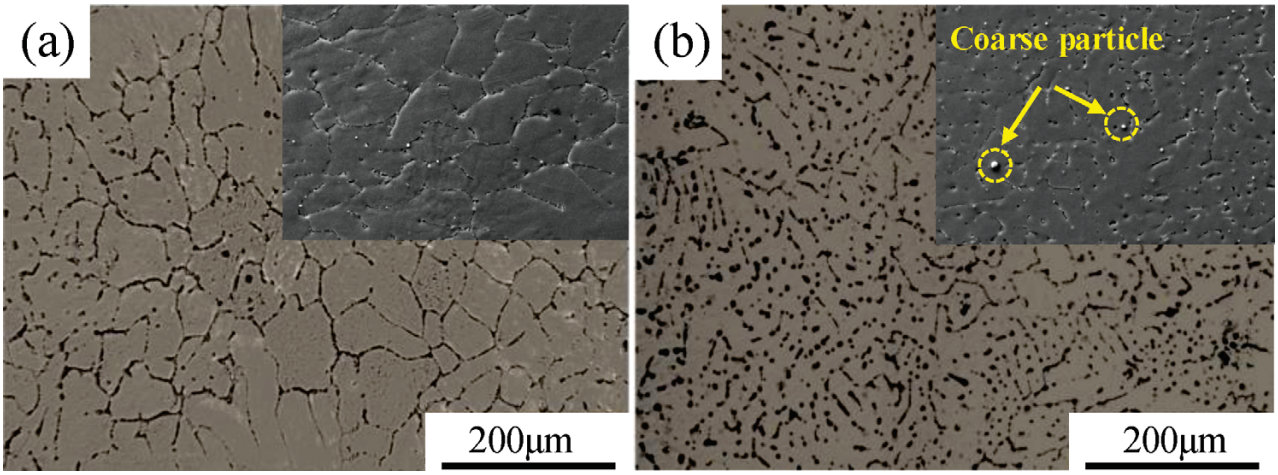

Figure 7: Microstructure at 350 °C and 0.001 s^{-1} at true strain of 0.25: a) XM10 alloy, b) XME100 alloy

cording to the study[24] and the EDS analysis, the finely distributed precipitates in the XM10 alloy and the coarse second-phase particles in the XME100 alloy are Mg_2Ca particles, which indicates that with the addition of Ce, the precipitation of Ca is promoted, resulting in the growth of the Mg_2Ca particles.

Figure 7 shows the microstructures of the deformed XM10 and XME100 alloys. It can be seen from **Figures 7a** and **7b** that the grains in the XM10 alloy were transformed into uniform equiaxial grains when the true strain is 0.25, which means that the alloy underwent DRX under this strain. Nevertheless, the volume fraction of DRX grains in the XME100 alloy is less than that of the XM10 alloy. And many elongated grains were found in the XEM100 alloy, which means that the alloy is incompletely DRX. The great number of coarse grains present in the XEM100 alloy may be able to accommodate more strain during the deformation, resulting in better machinability. As the SEM pictures of **Figures 7a** and **7b** show, the fine second-phase particles distributed at the grain boundaries in the XM10 alloy after deformation disappear. In contrast, many fine and coarse second phases distributed on grain boundaries can still be observed in the XME100 alloy. Thus, Ce prevents the dissolution of elements during the deformation and reduces the solubility of Ca in the alloy.

The pinning effect of the homogenous fine particle is beneficial to maintaining its deformed grains under high strains. The occurrence of DRX will be hindered if the drive energy of the deformation is equal to that of the pinning energy. It is seen from **Figure 7b** that the pinning of precipitates not only hinders the rearrangement of dislocations, but also hinders the movements of the sub-grain boundaries, inhibiting the nucleation of continuous DRX.[25] J. D. Robson et al.[26] found that DRX grains were rarely observed around the coarse particle. The DRX grains would appear occasionally around the large coarse-grain clusters of an individual deformed microstructure, but the effect of these grains on the total DRX can be ignored. Therefore, the PSN of DRX is retarded by the combined action of densely distributed fine particles and coarse particles, leading to the phenomenon of peak receding.

4 CONCLUSIONS

1. The alloy curve shows typical thermomechanical deformation behavior. The XME100 alloy has higher flow stress and a peak lagged effect at 0.001 s^{-1} strain rate. The peak lagged effect was due to the addition of Ce, promoting the precipitation of the second phase, which pins on the grain boundary and offsets a part of the deformation driving force, resulting in the weakening of the dynamic recrystallization ability.

2. The hot-processing parameter of the XME100 alloy exerts a great influence on the power-dissipation efficiency. The higher power-dissipation region is mainly at a deformation temperature between 320 °C and 360 °C and the strain rate below 0.004 s^{-1}. The lower power dissipation region is mainly when the temperature is between 300 °C and 360 °C above 0.018 s^{-1}.

3. There are two processing regions in the XME100 alloy: stable region I is at 300–450 °C and strain rate is less than 0.004 s^{-1}; stable region II is at 400–450 °C and strain rate is 0.0035–0.5 s^{-1}. To adapt to the actual industrial production, the optimal processing region is the stable region II, the temperature is 400–450 °C, the strain rate is 0.0035–0.5 s^{-1}.

Acknowledgments

The authors acknowledge support from National Natural Science Foundation of China (U1910213), Taiyuan University of Science and Technology Scientific Research Initial Funding (Grant No. 20202039)

5 REFERENCES

[1] D. M. Hong, D. Wu, R. S. Chen, X. H. Du, Ductility enhancement of EW75 alloy by multi-directional forging, J. Magnes. Alloy., 2 (**2014**) 4, 317–324, doi:10.1016/j.jma.2014.11.005

[2] T. Z. Han, G. S. Huang, Y. G. Wang, G. G. Wang, Y. C. Zhao, F. S. Pan, Enhanced mechanical properties of AZ31 magnesium alloy sheets by continuous bending process after V-bending, Prog. Nat. Sci., 26 (**2016**) 1, 97–102, doi:10.1016/j.pnsc.2016.01.005

[3] J. She, F. S. Pan, W. Guo, A. T. Tang, Z. Y. Gao, S. Q. Luo, K. Song, Z. W. Yu, M, Rashad, Effect of high Mn content on development of ultra-fine grain extruded magnesium alloy, Materials and Design., 90 (**2016**), 7–12, doi:10.1016/j.matdes.2015.10.093

[4] T. T. Tong, F. Zhang, S. H. Liu, Y. Du, K. Li, Experimental investigation on the phase equilibria of the Mg-Sn-Ag system in the Mg-rich corner, J. Magnes. Alloy., 5 (**2017**) 1, 41–47, doi:10.1016/j.jma.2017.02.003

[5] H. W. Jiang, F. Li, X. Zeng, Microstructural characteristics and deformation of magnesium alloy AZ31 produced by continuous variable cross-section direct extrusion, J Mater Sci Technol., 33 (**2017**) 6, 573–579, doi:10.1016/j.jmst.2017.01.003

[6] J. Zhao, B. Jiang, Y. Yuan, A. Tang, Q. Wang, T. Yang, G. Huang, D. Zhang, F. S. Pan, Influence of Ca and Zn synergistic alloying on the microstructure, tensile properties and strain hardening of Mg-1Gd alloy, Mater. Sci. Eng. A., 785 (**2020**), 139344, doi:10.1016/j.msea.2020.139344

[7] Q. Kang, H. T Jiang, Y. Zhang, Z. Xu, Z. Xia, Effect of various Ca content on microstructure and fracture toughness of extruded Mg-2Zn alloys, J. Alloys Compd., 742 (**2018**), 1019–1030, doi:10.1016/j.jallcom.2017.11.276

[8] Z. T. Li, X. G. Qian, C. Xu, X. Q. Liu, M. Y. Zheng, Enhanced strength by precipitate modification in wrought Mg–Al–Ca alloy with trace Mn addition, J. Alloys Compd., 836 (**2020**), 154689, doi:10.1016/j.jallcom.2020.154689

[9] Y. Z. Du, M. Y. Zheng, B. L. Jiang, Comparison of microstructure and mechanical properties of Mg-Zn microalloyed with Ca or Ce, Vacuum., 151 (**2018**), 221–225, doi:10.1016/j.vacuum.2018.02.029

[10] J. Sun, J. H. Li, P. Wang, Z. Y. Huang, Hot deformation behavior, dynamic recrystallization and processing map of Fe–30Mn–10Al–1C low-density steel, Trans. Indian Inst. Met., 75 (**2021**) 3, 699–716, doi:10.1007/s12666-021-02462-9

[11] Y. B. Yang, Q. F. Qin, Z. M. Zhang, Q. W. Wang, H. Hu, Processing maps of extruded AZ80 + 0.4% Ce magnesium alloy, J. Alloys Compd., 844 (**2020**), 156064, doi:10.1016/j.jallcom.2020.156064

[12] S. C. Sutton, A. A. Luo, Constitutive behavior and processing maps of a new wrought magnesium alloy ZE20 (Mg-2Zn-0.2Ce), J. Magnes. Alloy., 8 (**2020**) 1, 111–126, doi:10.1016/j.jma.2019.11.007

[13] C. C. Sun, K. Liu, Z. H. Wang, S. B. Li, X. Du, W. B. Du, Hot deformation behaviors and processing maps of Mg-Zn-Er alloys based on Gleeble-1500 hot compression simulation, Transactions of Nonferrous Metals Society of China., 26 (**2016**) 12, 3123–3134, doi:10.1016/S1003-6326(16)64444-8

[14] J. Li, J. Liu, Z. Cui, Characterization of hot deformation behavior of extruded ZK60 magnesium alloy using 3D processing maps, Mater. Des., 56 (**2014**), 889–897, doi:10.1016/j.matdes.2013.11.037

[15] Y. C. Lin, L. Li, Y. Xia, Y. Jiang, Hot deformation and processing map of a typical Al–Zn–Mg–Cu alloy, J. Alloys Compd., 550 (**2013**), 438–445, doi:10.1016/j.jallcom.2012.10.114

[16] W. Jia, S. Xu, Q. Le, F. Li, L. Ma, Modified Fields–Backofen model for constitutive behavior of as-cast AZ31B magnesium alloy during hot deformation, Mater. Des., 106 (**2016**), 120–132, doi:10.1016/j.matdes.2016.05.089

[17] C. Zhi, L. Ma, W. Jia, X. Huo, Z. Huang, Dependence of deformation behaviors on temperature for twin-roll casted AZ31 alloy by processing maps, J. Mater. Res. Technol., 8 (**2019**) 6, 5217–5232, doi:10.1016/j.jmrt.2019.08.044

[18] J. D. Robson, D. T. Henry, B. Davis, Particle effects on recrystallization in magnesium–manganese alloys: Particle pinning, Mater. Sci. Eng. A., 528 (**2011**) 12, 4239–4247, doi:10.1016/j.msea.2011.02.030

[19] X. Chen, F. Pan, J. Mao, J. Wang, D. Zhang, Effect of heat treatment on strain hardening of ZK60 Mg alloy, Mater. Des., 32 (**2011**) 3, 1526–1530, doi:10.1016/j.matdes.2010.10.008

[20] U. F. Kocks, H. Mecking, Physics and phenomenology of strain hardening: the FCC case, Prog. Mater. Sci., 48 (**2003**) 3, 171–273, doi:10.1016/S0079-6425(02)00003-8

[21] J. Feng, H. F. Sun, J. C. Li, X. W. Li, J. Zhang, Tensile flow and work hardening behaviors of ultrafine-grained Mg-3Al-Zn alloy at elevated temperatures, Mater. Sci. Eng. A., 667 (**2016**), 97–105, doi:10.1016/j.msea.2016.05.005

[22] T. Liu, F. Pan, X. Zhang, Effect of Sc addition on the work-hardening behavior of ZK60 magnesium alloy, Mater. Des., 43 (**2013**), 572–577, doi:10.1016/j.matdes.2012.07.050

[23] J. She, S. B. Zhou, P. Peng, A. T. Tang, H. C. Pan, C. L. Yang, F. S. Pan, Improvement of strength-ductility balance by Mn addition in Mg–Ca extruded alloy, Mater. Sci. Eng. A., 772 (**2020**), 138796, doi:10.1016/j.msea.2019.138796

[24] Z. T. Li, X. G. Qiao, C. Xu, X. Q. Liu, M. Y. Zheng, Enhanced strength by precipitate modification in wrought Mg–Al–Ca alloy with trace Mn addition, J. Alloys Compd., 836 (**2020**), 154689, doi:10.1016/j.jallcom.2020.154689

[25] Q. Wu, H. G. Yan, J. H. Chen, W. J. Xia, M. Song, B. Su, The interactions between dynamic precipitates and dynamic recrystallization in Mg-5Zn-1Mn alloys during hot compression, Mater. Charact., 160 (**2020**), 110131, doi:10.1016/j.matchar.2020.110131

[26] J. D. Robson, D. T. Henry, B. Davis, Particle effects on recrystallization in magnesium–manganese alloys: Particle-stimulated nucleation, Acta Mater., 57 (**2009**) 9, 2739–2747, doi:10.1016/j.actamat.2009.02.032